Multi Objective Optimisation of Metal Die Support Incremental Sheet Forming of SS 316L Sheets using Taguchi Grey Relational Analysis

Visagan ARJUNAN *, Ganesh PASUPATHY

Department of Production Technology, MIT Campus, Anna University, Chennai–600044, Tamil Nadu, India

http://doi.org/10.5755/j02.ms.38056

Received 29 July 2024; accepted 15 November 2024

The Metal Die Support Incremental Sheet Forming (MDS-ISF) enhances the dimensional accuracy of produced items in many industrial applications. However, the procedure limits metal sheet formability due to the strain between the tool and mandrel. As a result, selecting the best MDS-ISF technique to improve formability is a critical problem in the manufacture of complicated components. This study aims at optimising the forming parameters of MDS-ISF by forming single-walled cones of fixed wall angle and forming height by using Taguchi Grey Relational Analysis. The forming parameters selected for experimentation are step depth, spindle speed, and feed rate at three different levels. The responses, such as average surface roughness and average thickness, were selected for multi-objective optimisation and ANOVA was also conducted to study the influence of each forming parameter on the output responses. Additionally, the wall angle, and thickness of the components were also measured. From ANOVA, step depth had the uppermost influence on the surface finish and thickness trailed by feed rate and spindle speed.

Keywords: metal forming, surface roughness, thickness, optimisation, ANOVA.

1. INTRODUCTION

The traditional metal forming process has increased due to mass production. However, during the last decade due to market demand, lesser manufacturing time, and low flexibility the existing incremental forming process could not be supported, and it was not feasible to operate to meet the industrial needs. To extend the flexibility of incremental forming, many techniques have been developed to reduce the geometrical errors, and spring back effects and to get near net shape which can be achieved. [1]. Incremental to forming is used in batch production and is essentially a scientific procedure, where machines are specifically developed forming the required shapes. Simple tools like a fixture to clamp the sheet and a hemispherical tool to deform the sheet into the desired shape may be used to incrementally build symmetrical and asymmetrical forms [2]. In general, TPIF will be different from SPIF. It will have a partial or full die, and the blank that holds the workpiece will be angled in the direction of forming. [3]. TPIF is an improvement to SPIF that makes the limits for dimensions better. When TPIF is used, a full or partial die is used to shape the sheet metal in steps between two set points [4]. The parts made by TPIF were more accurate in terms of geometry than those made by SPIF because SPIF parts had less elastic rebound after being loaded [5].

Mohanraj Murugesan et al. [6] performed incremental sheet forming by varying forming parameters such as radius of the forming tool, spindle speed, step down, and feed rate. Taguchi L16 orthogonal array and Response Surface Methodology was used to optimise the surface finish of the formed components. The most influential parameter contributing to the improved surface finish was identified using ANOVA. The surface roughness was found to be decreasing when the step depth was decreased with increased feed rate. There was a significant reduction in surface roughness when the forming was performed at a decreased vertical step down and an increase in the feed rate and radius of the forming tool. The most influencing parameter on surface roughness was step down trailed by feed rate and radius of forming tool. H Zhu et al. [7] performed a simulation on positive and negative two points incremental forming. The simulated results such as thickness, profile curve, and equivalent strain of both methods were compared. The research indicates that the thickness, equivalent strain, and contour accuracy of the positive two-point incremental forming are superior to those of the negative two-point incremental forming process. Results showed that the positive two-point incremental forming exhibits superior forming quality when compared to negative incremental forming. The strain from the positive two-point incremental forming is spread out more evenly than the strain from the negative two-point incremental forming. The accuracy in measuring contours of the positive two-point incremental forming is better than that of the negative two-point incremental forming. M. Safari [8] performed incremental forming by varying process parameters such as, step depth and the tool's rotational speed affect the suggested specimen's highest possible outer and inner heights. By reducing the step depth and increasing the rotational speed of the tool, the maximum attainable outer and inner heights of the specimen were increased. However, the most significant impact was observed on the maximum achievable outer height. The highest attainable inner height of the specimen was most affected by the negative/positive variant of the sequence of positive and negative formation processes. In order to

* Corresponding author. Tel.: +91-9003270523.
E-mail: *avisagan69@mitindia.edu* (A. Visagan)

achieve the highest possible outer and inner heights, the S/N ratio analysis was used to determine the optimal combination of parameters.

Hani Mostafanezhad et al. [9] conducted TPIF of aluminum 1050 by varying forming parameters like die angle, the radius of the forming tool, the thickness of the sheet, and step down. The Box Bhenken experimental design was used to study and optimise the influence of the forming parameters on the ratio of thinning and maximum resultant force. The hierarchy of the highest contributing parameter was identified by ANOVA method. The angle of the die was the most influencing parameter on the thinning ratio on the other hand the thickness of the sheet considered had the maximum influence on the forces developed during the process. The thickness was found to be reduced at the wall regions of the components formed. Adham E. Ragab [10] performed a test on TPIF of A1050-H14 commercial aluminum sheets and studied the accuracy of the formed components. The parameters that were considered for optimisation are the diameter of the forming tool, rate of feed, step depth, and thickness of the formed sheets. The significance of each parameter on the accuracy of the formed components was studied using ANOVA. The higher the thickness of the sheet selected yielded better profile accuracy, and a lower feed rate improves the waviness at the walls of the formed components. The forming depth achieved was accurate for a lower feed rate of 500 mm/min and for having a better side wall angle a tool of diameter 15 mm is suggested. The overall accuracy of the process was found to be highly influenced by the thickness of the sheet selected for the forming process. Xiaoqiang Li et al. [11] performed TPIF on aluminum AA5052 to form a square cone and analysed the influence of tool-path strategy on thickness distribution. Four different forming strategies were employed and the best forming strategy was selected by comparing the thickness and change in strain of the formed components. The variable angle straight lines tool-path gave a higher thickness distribution when compared to the other suggested forming strategies. In the parallel linear tool-path strategy, the flange area of the final shape has been reduced in the first stage to make the slope of the specimen thicker at the wall region. However, as the stage number goes up, the thickness of the formed slope wall still goes down within a certain range because of the tension of the forming area.

M. Esmailian [12] et al. performed TPIF and generated an equation for the prediction of forming forces applied to the forming tool. Forming parameters such as coefficient of friction, dimensions of a sheet, a diameter of the tool, sheet thickness, sheet material, and the values of the yield stress of the sheet, friction coefficient, tool radius, and thickness of the sheet were selected as output responses. When the wall angle of the forming component is increased the local strain increases and the thickness variation increases, therefore the force applied to the forming tool is improved. Costel Catalin Coman [13] et al. studied the variations in forming forces, thinning effect, geometrical accuracy, and surface roughness of TPIF Al 3003 for a pyramidal trunk shape. The hardening process increases the forces generated and the TiN coated tool produced considerably lesser forming forces during forming.

The forming process creates deviations from the drawing, including shape deviations, as indicated by the radius of curvature of the side wall, the radius of connection between the wall and bottom, and dimensional deviations expressed by forming depth variation. The surface quality of the formed components was increased while the forming was performed using TiN coated tools. Umit Onal et al. [14] performed multistage TPIF on a DC04 sheet with a thickness of 0.98 mm by varying step depth, feed rate, clamping pressure, and angle increment. The target of the component to be formed was axially symmetrical with a 90° wall angle. The thickness of the wall angle was best when the angle of increment was kept at an interval of 100 between each pass. The clamping pressure when kept at 5.5 bar gave better thickness at the wall region. The thinning effect was highly experienced at the nose region of the components formed. The minimum thickness attained with the selected forming strategy and forming process was 0.34 mm.

Na Xue et al. [15] investigated the surface roughness, thickness, microstructure, and adhesion of Cooer graphite and copper coatings deposited on AZ31B and 6061 T6 magnesium and aluminium alloy under different spraying conditions were studied. The adhesion of the coatings applied on the AZ31B magnesium alloy substrate is generally greater than that on the 6061 T6 aluminum alloy substrate when the same spraying parameters are used. As the particle velocity increases, the Ra of the coatings sprayed on both soft and hard substrates decreases, whereas the thickness and adhesion of the coatings sprayed on both substrates increase. Ling Shao et al. [16] optimised the process parameters of cold-sprayed coatings by measuring responses such as surface roughness, thickness and adhesion. The surface roughness (*R*a) of the cold-sprayed coatings gradually decreases as the gas pressure, and temperature increase. The thickness of the deposited coatings increases significantly as the gas pressure and temperature increase.

Yuhong Zhao et al. [17] studied the morphological evolution, volume fraction, elastic strain energy effect, composition distribution, enthalpy of formation, interface energy and electron localization function, and the stability or instability of various metastable of various phase boundaries in the selected material. The formation enthalpy and interfacial energy show that all four PBs are stable, with A/B2 having lower energy than A/B1, driving the transformation. A/CD is the most stable, and interface stability decreases in the order: A/B1 > A/B2 > A/E > A/CD. Sunwu Xu et al. [18] explored the use of composite solder joints, specifically a novel combination of SAC (Sn-3Ag-0.5Cu) and Sn-Pb (Sn-37Pb), to enhance the mechanical reliability of Package-on-Package (PoP) technology, which supports Moore's Law. The formation and phase distribution of the composite joint depends on reflow temperature, with optimal results observed at 200 °C and 60 seconds dwell time when 10 wt.% Sn-Pb is used. Finite element simulations showed a 29 % reduction in maximum stress compared to full SAC joints. Jinhong Liu et al. [19] conducted an in-situ TEM study of a micro-Cu/ENIG/Sn solder joint under an isothermal aging test. During ultrasonic bonding, η-Cu6Sn5 intermetallic compounds (IMCs) formed in the solder joint

due to copper diffusion from the electrode. As the joint was heated to 100 °C, Sn enriched regions diffused and reacted with elements to form (NixCu1-x)3Sn4, AuSn4, and Cu6Sn5, while Cu6Sn5 developed a scallop-like morphology. A phase transition between η and η' phases of Cu6Sn5 occurred near 186 – 189 °C, which involved a three-stage process, potentially causing cracks due to volume changes.

Tang Yu et al. [20] proposed an improved CNN for detecting forging defects, using EfficientNet, Feature Pyramid Network (FPN), and Particle Swarm Optimization (PSO). The high-level semantic features are incorporated into the FPN fusion layer, effectively enhancing the model's multi-scale object detection capabilities. The model achieved high accuracy with a 95.69 % mean Average Precision (mAP) and 0.94 F1 score, outperforming other models in efficiency and defect detection. Wei Zhang et al. [21] proposed a simple, accurate method for calibrating measurement sensitivity in a phase-shifting shadow moire system. By adjusting the illumination angle and analyzing fringe pattern variations, the system's sensitivity is calibrated. Validation experiments showed a reliable measurement accuracy with a standard deviation of 0.698 μm and 0.7 % error at 98.21 μm sensitivity.

Zili Wang et al. [22] proposed a six-axis free-bending (FB) processing and springback prediction in spiral tubes, crucial for aerospace fluid transport systems. It introduces a novel FB method and a physics-informed neural network (PINN)-based model that integrates an improved theoretical approach. The PINN model, comprising three sub-networks, outperforms traditional methods in five evaluation metrics (ED, DTW, LCSS, FD, MD) and accurately predicts curvature and torsion, enhancing theoretical predictions. Gangqiang Kong et al. [23] investigated the dynamic behavior of ballastless track XCC pile-raft foundations subjected to varying axle loads through an experimental study. The focus is on the dynamic soil stresses and velocity responses under vertical cyclic loading. Key findings include that the dynamic soil stresses on the subgrade surface form an "ω" shape, while those on the subsoil surface form a "U" shape.

Jie Li et al. [24] presented a novel diameter-adjustable mandrel (DAM) designed to improve the metal tube bending process by adapting to tubes of varying diameters, addressing issues such as high costs, long design cycles, and low reuse rates associated with traditional mandrels. Featuring a multi-point contact design, the DAM can cause irregular cross-section deformation, which is evaluated using the cross-sectional full profile radial error (FP-RE) model. Experiments with AISI 304L tubes (40 – 56 mm inner diameter) showed a maximum FP-RE error of 0.11 % compared to FEA results. The DAM, with a minimum effective diameter of 40 mm and six support blocks, proved effective for tubes with inner diameters of 40 to 56 mm, maintaining acceptable forming quality.

Yongzhe Xiang et al. [25] performed Rotary Draw Bending using a tangential variable boosting (TVB) to analyse the defects during the process. To assess the effects of TVB, a parameter-weight-adaptive convolutional neural network (PWA-CNN) was developed to predict cross-sectional defects. The prediction model was trained using a dataset generated from numerical simulations of aluminum-alloy tubes, and its performance was compared with other CNNs and weight assignment methods. Results showed that the PWA-CNN outperformed other methods in predicting tube cross-sectional distortion.

Lin Hua et al. [26] investigated the mechanism of void healing in cold-rolled aeroengine M50 bearing steel subjected to electroshocking treatment (EST) through experimental and simulation approaches. Using three-dimensional X-ray microscopy (3D-XRM), it was observed that the porosity of the cold-rolled samples decreased from 0.26 % to 0.09 % after EST, with smaller voids healing more effectively than larger ones. Simulations revealed that an inhomogeneous physical field generates high local thermal compressive stress, up to 2565.9 MPa, around ellipsoidal voids, driving the healing process. Qimeng Zhu et al. [27] analyzed the impact of microstructures on the velocity and stress coefficient (K) of longitudinal critically refracted (LCR) waves for measuring welding residual stress, enhancing the traditional LCR wave method. The proposed LCR-AV (attenuation velocity) method was tested on A7N01 welded joints, considering grain size variations from heat treatments. Findings show that voltage amplitude changes linearly with velocity and stress coefficient, independent of precipitation effects.

Qiang Gong et al. [28] examined the impact of abrasive particles on the workpiece load during machining, focusing on stress tensor, yield performance, and third invariant. The results showed that while grinding parameter variations have minimal impact on the stress applied by a single abrasive grain, they significantly affect the stress load range, concentrating stress at the removal endpoint. The front end of abrasive grains shows yield deformation, and the bottom shows tensile deformation. The Element diffusion at high temperatures and strain rates increases subsurface microhardness by about 15 μm.

In this study MDS-ISF was performed on SS 316L sheets of uniform thickness by varying forming parameters such as step depth, spindle speed and feed rate. The target geometry was a single wall angle cone of 66° with a forming height of 60 mm. Taguchi GRA was selected for optimising the process parameters to get better thickness and surface roughness. The geometry of the formed components was measured using CMM and the comparison was made for different step depths.

2. EXPERIMENTAL WORK

A single wall angle cone having a fixed wall angle of 66° and a constant forming height of 60 mm has been taken as the target shape and was designed using SolidWorks 2018. The MDS-ISF experiments were performed in a 3 axis multi–CNC Vertimach Tal V-510 milling machine. 316L stainless steel (SS 316L) is the most frequently used chromium-nickel stainless steel grade and has a broad variety of industrial applications, including chemical equipment, cooling coils, nuclear vessels, components etc. [29]. SS 316L stainless sheets were prepared for a dimension of 280 mm × 280 mm. Fig. 1 shows the fabricated MDS-ISF fixture used for holding the workpiece during the forming process. For the forming process, a carbide tool with a 12 mm diameter and a 150 mm shank length was chosen. The forming parameters and their levels are given in Table 1.

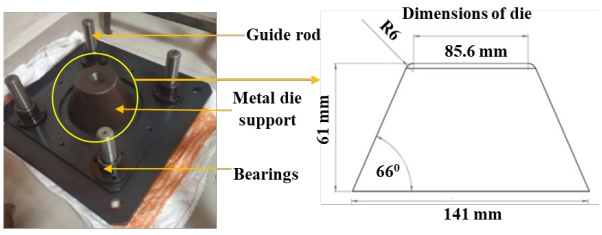

a

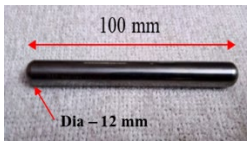

b

Fig. 1. a – MDS-ISF fixture; b – forming tool

Table 1. Forming parameters and their levels

Forming parameter	Symbol	Units	Level 1	Level 2	Level 3
Step depth	SD	mm	0.2	0.3	0.4
Spindle speed	SS	rpm	100	200	300
Feed rate	FR	mm/min	500	1000	1500

Table 2. Experimental layout and the response variables using L_9 OA

Exp No.	SD	SS	FR	Avg *Ra* (Ra_{avg})	Avg *Th* (Th_{avg})
1	0.2	100	500	0.594	0.516
2	0.2	200	1000	0.623	0.524
3	0.2	300	1500	0.534	0.536
4	0.3	100	1000	0.615	0.561
5	0.3	200	1500	0.556	0.537
6	0.3	300	500	0.646	0.556
7	0.4	100	1500	0.545	0.542
8	0.4	200	500	0.564	0.525
9	0.4	300	1000	0.572	0.531

3. RESULTS AND DISCUSSION

3.1. Grey relational analysis

Taguchi's Grey relational analysis effectively optimizes the input parameters, thereby reducing the number of orthogonal array tests required [30]. Grey relational analysis is a very effective statistical analysis approach used to address situations with intricate relationships and various elements and variables. Integrating all the contributing attributes into one single combined attribute is an idea of the solution. The Taguchi L_9 orthogonal array was designed to conduct the experiments, and the sample of the formed components is shown in Fig. 2. The responses considered for optimization were average surface roughness and average thickness of the formed components. The experimental layout and the obtained results are shown in Table 2. The first stage is to calculate the S/N ratio~~n~~ and normalize the multiple responses or attributes considered into one single attribute. The next step is to calculate the Grey Relation Coefficient (GRC), and finally the Grey Relational Grade (GRG).

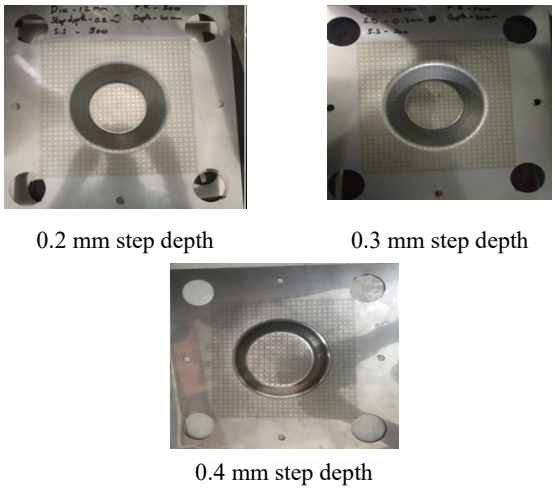

Fig. 2. Sample of MDS-ISF components at different step depths: a – top view; b – front view

In general, larger GRG values indicate better output qualities [31]. The validation experiments were performed by using the optimum process parameter combination obtained and the results were measured.

3.2. S/N ratio normalizing the results

Grey relational analysis makes appropriate use of the normalized raw data acquired from experiments. The signal-to-noise ratio quantifies the extent to which the response deviates from the nominal or target value in the presence of various noise conditions. The roughness of the surface was considered as smaller the better and the thickness was considered as larger the better criterion. The S/N ratio of the output responses are calculated using Eq. 1 and Eq. 2 respectively and shown in Table 3.

Smaller the better, $$A_{ij} = -10\log_{10}\left(\frac{1}{n}\right)\sum_{i=1}^{n}(b_{ij^2}); \qquad (1)$$

Larger the better, $A_{ij} = -10\log_{10}\left(\frac{1}{n}\right)\sum_{i=1}^{n}(1/b_{ij^2})$, (2)

where n represents the number of replications and A_{ij} is the response of the respective experiments.

To produce a single objective function, it is necessary to normalize the objective functions. This is because the multiple objectives might be combined with different units. The obtained results of incrementally formed sheets were linearly normalised so that they fit in between 0 and 1.

The normalisation for output responses is calculated using Eq. 3 and Eq. 4 respectively. The normalised values of average surface roughness and average thickness are shown in Table 3.

Smaller the better, $N_{ij} = \frac{(MaxA_{ij} - A_{ij})}{(Max\ A_{ij} - Min\ A_{ij})}$; (3)

Larger the better, $N_{ij} = \frac{(A_{ij} - MinA_{ij})}{(Max\ A_{ij} - Min\ A_{ij})}$. (4)

Table 3. S/N ratio, normalised S/N ratio of MDS-ISF components

Exp No.	S/N ratio		Normalised S/N ratio	
	*R*a avg	*Th* avg	*R*a avg	*Th* avg
1	4.519	–5.747	0.5622	0.0000
2	4.106	–5.613	0.8124	0.1853
3	5.449	–5.417	0.0000	0.4581
4	4.227	–5.026	0.7389	1.0000
5	5.099	–5.401	0.2120	0.4805
6	3.795	–5.099	1.0000	0.8993
7	5.267	–5.325	0.1103	0.5847
8	4.974	–5.591	0.2871	0.2159
9	4.852	–5.493	0.3610	0.3527

3.3. Grey relational coefficient

The difference between the normalised and the ideal results can be obtained by calculating the value of GRC by using Eq. 5 and shown in Table 4. The normalized values are closer to the ideal result when the value of the corresponding GRC is higher. The aim of the differentiating coefficient is to modify the range of the GRC, allowing for adjustment according to specific requirements. The rank of all the GRC derived using distinguishing coefficients would not change even if various distinguishing coefficients would provide different results.

For GRC, $\varphi_{ij} = \frac{N_{\min} + \lambda N_{\max}}{N_{ij} + \lambda N_{\max}}$, (5)

where λ is the distinguishing coefficient, $(0 \le \lambda \le 1)$, in the current case it is taken as 0.5.

3.4. Grey relational grade

The GRG is calculated by averaging the coefficients for each measured output response. The GRG is calculated by using Eq. 6 and the values are shown in Table 4.

$$GRG_i = \frac{1}{m}\sum_{j=1}^{m}\varphi_{ij}\ . \quad (6)$$

The GRG evaluates the importance of each performance feature on the experiment's result. Furthermore, this would provide us with valuable information on the optimal level of the performance characteristics in order to get the highest potential output. The higher the GRG number, the more influential the process parameter becomes [32]. The optimum process parameter combination as shown in Table 5 for getting higher thickness and lower surface roughness is step depth (SD – 0.3 mm), spindle speed (SS – 300 rpm) and feed rate (1000 mm/min). i.e $SD_2SS_3FR_2$.The step depth was found to be the most influential parameter for obtaining better thickness and surface roughness.

Table 4. GRC, GRG and of MDS-ISF components

Exp No.	GRC		GRG	Rank
	*R*a avg	*Th* avg		
1	0.533	0.333	0.433	7
2	0.727	0.380	0.554	3
3	0.333	0.480	0.407	8
4	0.657	1.000	0.828	2
5	0.388	0.490	0.439	5
6	1.000	0.832	0.916	1
7	0.360	0.546	0.453	4
8	0.412	0.389	0.401	9
9	0.439	0.436	0.437	6

Table 5. Average GRG for each process parameter combination

Forming parameters	Average GRG				
	L 1	L 2	L3	Delta	Rank
SD	0.465	0.728	0.43	0.298	1
SS	0.572	0.465	0.587	0.122	3
FR	0.583	0.607	0.433	0.174	2

3.5. Validation of experiments

The optimal level of machining parameters that were obtained in the previous phase is crucial for predicting and verifying the enhancement of the performance characteristics. The predicted GRG can be obtained from Eq. 7.

$$Y = Y_i + \sum(Y_n - Y_i), \quad (7)$$

where Y_i is the mean GRG; Y_n is the mean GRG at optimal condition.

Table 6 shows the average surface roughness (Ra_{avg}) has significantly reduced from 0.594 µm to 0.512 µm and the average thickness (Th_{avg}) has considerably increased from 0.516 mm to 0.535 mm. The predicted result is experimentally validated and deviation was found to be within the acceptable range.

Table 6. Comparison results of the initial and optimum combination of process parameters

List of forming parameters	Initial machining parameters	Optimum machining parameters	
		Predicted	Optimum
Ra_{avg}, µm	0.594	0.583	0.512
Th_{avg}, mm	0.516	0.591	0.535
GRG	0.433	0.548	0.641

3.6. Analysis of variance

The most influencing forming parameter on the output responses can be identified using Analysis of Variance (ANOVA) as shown in Fig. 3. Table 7 shows the ANOVA for GRG where step depth (SD) had the uppermost contribution of 52.74 % trailed by feed rate (FR) of 17.66 % and spindle speed (SS) of 8.81 %.

Table 7. ANOVA for weighted GRG

Source	DF	Sum of square	Mean sum of square	Contribution
SD	2	0.15913	0.07956	52.74 %
SS	2	0.02658	0.01329	8.81 %
FR	2	0.05328	0.02664	17.66 %
Error	2	0.06271	0.03136	20.79 %
Total	8	0.30170	–	100.00 %

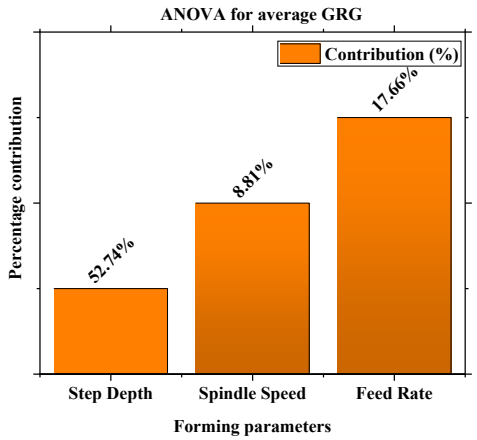

Fig. 3. ANOVA for average GRG

3.7. Geometrical study

Geometrical accuracy is found by comparing the profile of the formed sheet against the original CAD geometry. Fig. 4 shows the CAD vs Experimental plots for different step depths. The mean square error (MSE) calculated using Eq. 8 is used to quantify the accuracy of the formed sheet and the values obtained are given in Table 8 and same has been shown in Fig.5.

$$MSE = \frac{1}{n}\sum_{i=1}^{n}(y_i - \hat{y}_i)^2 \quad , \tag{8}$$

where n is the number of data points; y_i observed values; $\hat{y}_i$ are the CAD values.

3.8. Thickness distribution

To determine the thickness of the formed sheets, they were cut using wire-cut EDM. The initial thickness of the sheet before forming was 0.8 mm. Table 9 shows the thickness of the sheet measured using a digital micrometer after forming. The final thickness distribution of the formed sheets for different step depth is shown in Fig. 6. The minimum thickness of 0.224 mm was obtained for a Step depth of 0.2 mm, Tool rotational speed of 100 rpm ad feed rate of 500 mm/min (Experiment 1).

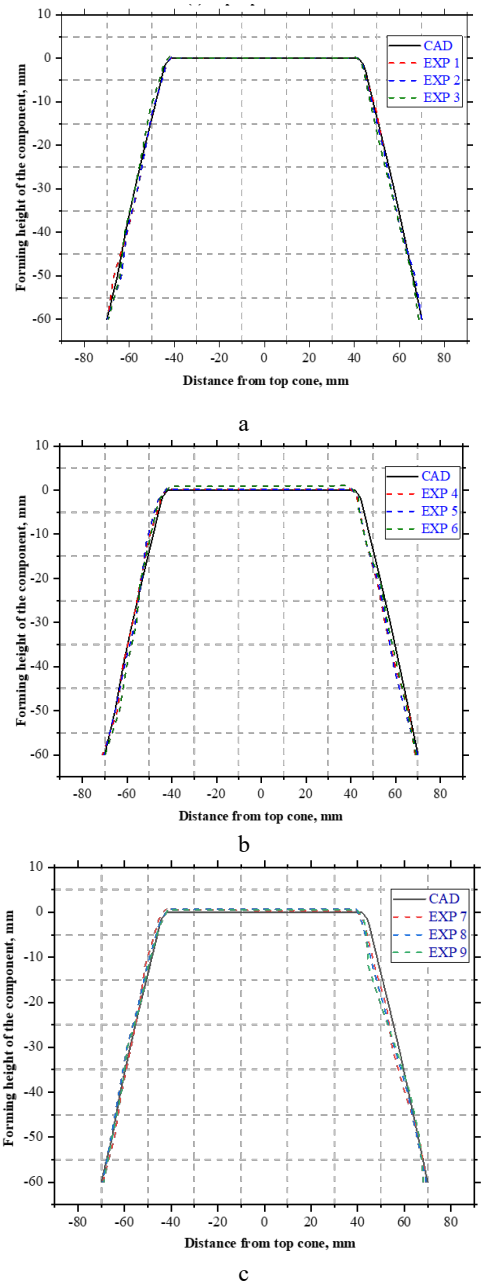

Fig. 4. a – profile plot for 0.2 mm step depth; b – profile plot for 0.3 mm step depth; c – profile plot for 0.4 mm step depth

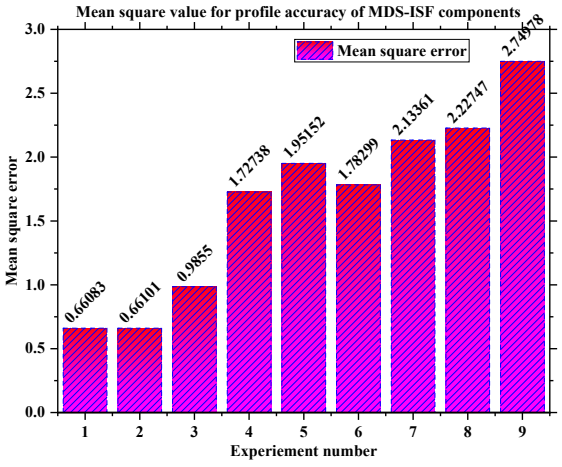

Fig. 5. Mean square value for profile accuracy of MDS-ISF components

Table 8. MSE values of EXP vs CAD each experimental combination

EXP vs CAD									
Exp no.	1	2	3	4	5	6	7	8	9
MSE	0.6608	0.66101	0.98550	1.72738	1.95152	1.78299	2.13361	2.22747	2.74978

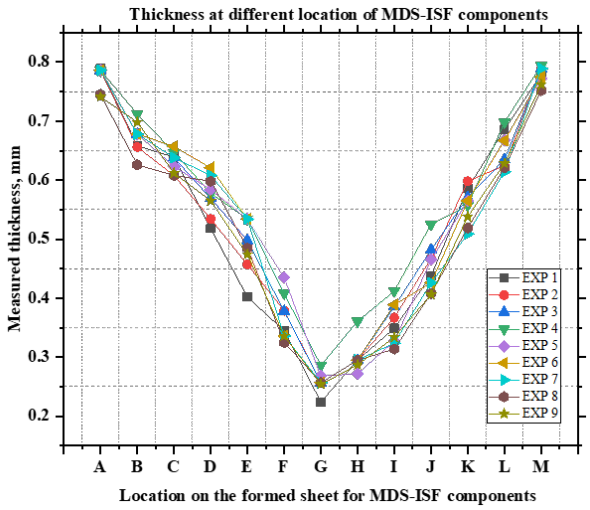

Fig. 6. Thickness at different locations on the formed sheet of MDS-ISF components

4. CONCLUSIONS

The effects of forming parameters on the surface roughness, geometrical accuracy and average thickness of MDS-ISF parts have been studied experimentally on SS 316L sheets of uniform thickness. Then, the process parameters were examined and optimized using the Taguchi technique considering the L9 orthogonal array average surface roughness and average thickness on SS 316L sheets of uniform thickness. The results of the current work are as follows:

1. The initial results showed that a better average surface roughness of 0.534 µm was achieved for a step depth of 0.2 mm, spindle speed of 300 rpm, and feed rate of 1500 mm/min. Similarly, a better average thickness of 0.561 mm was achieved at a step depth of 0.3 mm, spindle speed of 100 rpm, and feed rate of 1000 mm/min.
2. Taguchi L9 orthogonal array revealed that the optimum forming inputs for better surface finish and thickness were at a step depth of 0.3 mm, spindle speed of 300 rpm, and feed rate of 1000 mm/min.
3. The ANOVA results showed that step depth (SD) had the uppermost contribution of 52.74 % trailed by feed rate (FR) of 17.66 % and spindle speed (SS) of 8.81 %.
4. The accuracy of the formed components was better at lower step depths when compared to forming the components at higher forming step depths.
5. Validation tests were conducted at the optimum setting of forming parameter and there was a significant improvement in the obtained results, and hence Taguchi method proves a better way in optimising the process parameters of MDS-ISF of SS 316L with uniform thickness.

The present work is performed with a single wall angle die which shall be changed for a double varying wall angle die for future works. The FEA of the metal die support incremental sheet forming shall be carried out and the FEA vs Exp comparison on thickness and profile plots shall studied. The number of experiments shall be increased and different diameters of tools and their influence on the forming responses shall be studied.

REFERENCES

1. **Visagan, A., Ganesh, P.** Influence of Higher Wall Angle on Formability in Spif of AISI 316L *Journal of Advanced Microscopy Research* 13 2018: pp. 1 – 5. https://doi.org/10.1166/jamr.2018.1388
2. **Ganesh, P., Visagan, A., Ethiraj, N., Prabhakar, M., Sendilvelan, S.** Optimization of Pyramid Shaped Single Point Incremental Forming of AA5052 Alloy Sheet *Materials Today: Proceedings* 45 2021: pp. 5892 – 5898. https://doi.org/10.1016/j.matpr.2020.08.573

Table 9. Thickness distribution of MDS-ISF components

Location	Thickness, mm								
	EXP 1	EXP 2	EXP 3	EXP 4	EXP 5	EXP 6	EXP 7	EXP 8	EXP 9
A	0.789	0.786	0.786	0.786	0.786	0.786	0.786	0.745	0.741
B	0.658	0.656	0.678	0.712	0.678	0.678	0.678	0.626	0.698
C	0.639	0.608	0.638	0.647	0.623	0.657	0.638	0.608	0.612
D	0.518	0.534	0.569	0.578	0.584	0.621	0.608	0.598	0.565
E	0.402	0.457	0.498	0.534	0.534	0.534	0.534	0.485	0.474
F	0.345	0.379	0.378	0.408	0.435	0.336	0.336	0.325	0.336
G	0.224	0.257	0.257	0.286	0.268	0.257	0.257	0.257	0.254
H	0.295	0.295	0.295	0.361	0.272	0.295	0.295	0.295	0.287
I	0.349	0.367	0.386	0.412	0.327	0.389	0.324	0.314	0.334
J	0.438	0.467	0.482	0.525	0.465	0.426	0.426	0.408	0.406
K	0.586	0.598	0.571	0.557	0.565	0.565	0.509	0.519	0.538
L	0.686	0.625	0.635	0.698	0.668	0.667	0.614	0.621	0.628
M	0.779	0.789	0.789	0.794	0.772	0.775	0.789	0.752	0.762
Average	0.516	0.524	0.536	0.561	0.537	0.537	0.523	0.504	0.510

3. **Suriya, P., Keattipong, O.** The Optimization of Sheet Forming in Residual Stress and Surface Roughness with Two Point Incremental Forming Process (TPIF) of Aluminum Alloy Part *Applied Science and Engineering Progress* 16 (4) 2023: pp. 1 – 10. https://doi.org/10.14416/j.asep.2022.06.003
4. **Jeswiet, J., Micari, F., Hirt, G., Bramley, A., Duflou, J., Allwood, J.** Asymmetric Single Point Incremental Forming of Sheet Metal *CIRP Annals - Manufacturing Technology* 54 (2) 2005: pp. 623 – 649. https://doi.org/10.1016/S0007-8506(07)60021-3
5. **Silva, M.B., Martins, P.A.F.** Two-Point Incremental Forming with Partial Die: Theory and Experimentation *Journal of Materials Engineering and Performance* 22 2013: pp. 1018 – 1027. https://doi.org/10.1007/s11665-012-0400-3
6. **Mohanraj, M., Jae Hyeong, Y., Kyu Seok, J., Sung-Min, C., Krishna Singh, B., Chang-Whan, L.** Optimization of Forming Parameters in Incremental Sheet Forming of AA3003-H18 Sheets Using Taguchi Method *Materials* 15 2022: pp. 1 – 16. https://doi.org/10.3390/ma15041458
7. **Zhu, H., Cheng, G.X., Dong Won, J.** Comparison of the Positive and Negative Two Points Incremental Forming Quality *Journal of Physics: Conference Series* 1922 2021: pp. 1 – 9. https://doi.org/10.1088/1742-6596/1922/1/012012
8. **Safari, M.** Two Point Incremental Forming of a Complicated Shape with Negative and Positive Dies *Iranian Journal of Materials Forming* 4 (2) 2017: pp. 51 – 61. https://doi.org/10.22099/IJMF.2017.26486.1091
9. **Han, M., Hossein Ghorbani, M., Samad, E., Ehsan Marzban, S.** Optimization of Two-Point Incremental Forming Process of AA1050 through Response Surface Methodology *Measurement* 127 2018: pp. 21 – 28. https://doi.org/10.1016/j.measurement.2018.04.042
10. **Adham Ragab, E.** Multi-objective Optimisation of Profile Accuracy in Two Point Incremental Forming using Taguchi-based Grey Relation Analysis *International Journal of Collaborative Enterprise* 6 (1) 2018: pp. 49 – 65. https://doi.org/10.1504/IJCENT.2018.092093
11. **Xiaoqiang, L., Kai, H., Dongsheng, Li.** Multi-Stage Two Point Incremental Sheet Forming *Journal of Physics: Conference Series* 1063 2018: pp. 1 – 7. https://doi.org/10.1088/1742-6596/1063/1/012064
12. **Esmailian, E., Khalili, K.** Prediction of Tool Force in Two Point Incremental Forming by Slab Analysis *International Journal of Engineering* 33 (11) 2020: pp. 2399 – 2407. https://doi.org/10.5829/ije.2020.33.11b.30
13. **Costel Catalin, C., Simona Nicoleta, M., Constantin, C., Dumitru, N.** Analysis of Incremental Sheet Forming of Aluminum Alloy *Materials* 16 (6371) 2023: pp. 1 – 20. https://doi.org/10.3390/ma16196371
14. **Umit, O., Omer, S., Ibrahim, O., Aslan, C., Idris, C.** A New Approach to Multi-Stage Incremental Forming Method *Arabian Journal for Science and Engineering* 2024: pp. 1 – 10. https://doi.org/10.1007/s13369-024-08970-2
15. **Na, X., Weiwei, L., Ling, S., Zhibiao, T., Yingwei, C., Sheng, D., Nengyong, Y., Jitang, Z., Qijie, L., Jinfang, W., Meng, Z., Xinxing, S., Tianle, W., Mengliang, C., Yingqi, H., Feilong, X., Liu, Z.** 'Comparison of Cold-Sprayed Coatings of Copper-Based Composite Deposited on AZ31B Magnesium Alloy and 6061 T6 Aluminum Alloy Substrates *Materials* 16 2023: pp. 1 – 17. https://doi.org/10.3390/ma16145120
16. **Ling, S., Na, X., Weiwei, L., Song, L., Zhibiao, T., Yingwei, C., Jitang, Z., Sheng, D., Qijie, L., Xinxing, S., Tianle, W., Mengliang, C., Yingqi, H., Feilong, X., Liu, Z.** Effect of Cold-Spray Parameters on Surface Roughness, Thickness and Adhesion of Copper-Based Composite Coating on Aluminum Alloy 6061 T6 Substrate *Processes* 11 2023: pp. 1 – 15. https://doi.org/10.3390/pr11030959
17. **Yuhong, Z.** Stability of phase boundary between L12-Ni3Al phases: A phase field study *Intermetallics* 144 2022: pp. 1 – 9. https://doi.org/10.1016/j.intermet.2022.107528
18. **Sunwu, X., Xinyi, J., Pengyu, Z., Haoran, J., Kyung Wook, P., Peng, H., Shuye, Z.** Equilibrium Phase Diagram Design and Structural Optimization of SAC/Sn-Pb Composite Structure Solder Joint for Preferable Stress Distribution *Materials Characterization* 206 2023: pp. 1 – 11. https://doi.org/10.1016/j.matchar.2023.113389
19. **Jinhong, L., Jianhao, X., Kyung Wook, P., Peng, H., Shuye, Z.** In-situ Isothermal Aging TEM Analysis of a Micro-Cu/ENIG/Sn Solder Joint for Flexible Interconnects *Journal of Materials Science & Technology* 169 2024: pp. 42 – 52. https://doi.org/10.1016/j.jmst.2023.06.020
20. **Tang, Y., Wang, C., Gao, J., Hua, P.** Intelligent Detection Method of Forgings Defects Detection based on Improved Efficient Net and Memetic Algorithm *IEEE Access* 10 2022: pp. 79553 – 79563. https://doi.org/10.1109/ACCESS.2022.3193676
21. **Wei, Z., Fulong, Z., Shenghuai, W., Pengyan, L., Xin, W.** An Accurate Method to Calibrate Shadow Moiré Measurement Sensitivity *Measurement Science and Technology* 30 2019: pp. 1 – 8. https://doi.org/10.1088/1361-6501/ab1e2d
22. **Zili, W., Yongzhe, X., Shuyou, Z., Xiaojian, L., Jun, M., Jianrong, T., Le, W.** Physics-informed Springback Prediction of 3D Aircraft Tubes with Six-Axis Free-Bending Manufacturing *Aerospace Science and Technology* 147 2024: pp. 1 – 20. https://doi.org/10.1016/j.ast.2024.109022
23. **Gang Qiang, K., Guangchao, S., Hanlong, L., Jiliang, L.** Dynamic Response of Ballastless Track XCC Pile-Raft Foundation Under Train Axle Loads *Journal of testing and evaluation* 49 2021: pp. 1691 – 1704. https://doi.org/10.1520/JTE20180032.
24. **Jie, L., Zili, W., Shuyou, Z., Yaochen, L., Le, W., Chang, S., Jianrong, T.** A Novelty Mandrel Supported Thin-Wall Tube Bending Cross-Section Quality Analysis: A Diameter-Adjustable Multi-Point Contact Mandrel *The International Journal of Advanced Manufacturing Technology* 124 2023: pp. 4615 – 4637. https://doi.org/10.1007/s00170-023-10838-y
25. **Yongzhe, X., Zili, W., Shuyou, Z., Lanfang, J., Yaochen, L., Jianrong, T.** Cross-Sectional Performance Prediction of Metal Tubes Bending with Tangential Variable Boosting based on Parameters-Weight-Adaptive CNN *Expert Systems with Applications* 237 2024: pp. 1 – 17. https://doi.org/10.1016/j.eswa.2023.121465
26. **Lin, H., Yuling, L., Dongsheng, Q., Lechun, X., Feng, W., Min, W.** Mechanism of Void Healing in Cold Rolled Aeroengine M50 Bearing Steel under Electroshocking Treatment: A Combined Experimental and Simulation Study *Materials Characterization* 185 2022: pp. 1 – 15.

https://doi.org/10.1016/j.matchar.2022.111736

27. **Qimeng, Z., Jia, C., Guoqing, G., Hui, C., Peng, L.** Ameliorated Longitudinal Critically Refracted-Attenuation Velocity Method for Welding Residual Stress Measurement *Journal of Materials Processing Technology* 246 2017: pp. 267 – 275. https://doi.org/10.1016/j.jmatprotec.2017.03.022
28. **Qiang, G., Ming, C., Yadong, G., Minghui, C., Tao, Z., Qianqian, L.** Grinding Surface and Subsurface Stress Load of Nickel-Based Single Crystal Superalloy DD5 *Precision Engineering* 88 2024: pp. 354 – 366. https://doi.org/10.1016/j.precisioneng.2024.02.017
29. **Visagan, A., Ganesh, P.** Experimental Studies on Die based Two Point Incremental Forming *International Journal of Vehicle Structures & Systems* 14 (7) 2022: pp. 912 – 917. https://doi.org/10.4273/ijvss.14.7.17
30. **Visagan, A., Ganesh, P.** Parametric Optimization of Two Point Incremental Forming using GRA and TOPSIS *International Journal of Simulation Modeling* 21 (4) 2022: pp. 615 – 626. https://doi.org/10.2507/IJSIMM21-4-622
31. **Visagan, A., Ganesh, P.** A Hybrid Optimization Approach of Single Point Incremental Sheet Forming of AISI 316L Stainless Steel Using Grey Relation Analysis Coupled with Principal Component Analysis *Journal of Wuhan University of Technology-Material Science Edition* 39 2024: pp. 160 – 166. https: //doi. org/10.1007/s11595-024-2867-9
32. **Visagan, A., Ganesh, P., Ethiraj, N., Kalaichelvan, K.** Multi-Objective Optimization of Single Point Incremental Forming of 316L Stainless Steel using Grey Relational and Principal Component Analyses *Transactions of FAMENA* 48 (2) 2024: pp. 85 – 89. https://doi.org/10.21278/TOF.482054923